Published in final edited form as:

IEEE Trans Med Imaging. 2017 February ; 36(2): 574–583. doi:10.1109/TMI.2016.2622251.

A Millimeter-Wave Digital Link for Wireless MRI

Kamal Aggarwal,
Stanford University, Stanford, CA-94305, USA

Kiran R. Joshi,
Stanford University, Stanford, CA-94305, USA

Yashar Rajavi,
Stanford University, Stanford, CA-94305, USA

Mazhareddin Taghivand,
Stanford University, Stanford, CA-94305, USA. He is now with Qualcomm Inc, San Jose, CA-95110, USA

John M. Pauly,
Stanford University, Stanford, CA-94305, USA

Ada S. Y. Poon, and
Stanford University, Stanford, CA-94305, USA

Greig Scott
Stanford University, Stanford, CA-94305, USA

Abstract

A millimeter (mm) wave radio is presented in this work to support wireless MRI data transmission. High path loss and availability of wide bandwidth make mm-waves an ideal candidate for short range, high data rata communication required for wireless MRI. The proposed system uses a custom designed integrated chip (IC) mm-wave radio with 60 GHz as radio frequency carrier. In this work, we assess performance in a 1.5 T MRI field, with the addition of optical links between the console room and magnet. The system uses ON-OFF keying (OOK) modulation for data transmission and supports data rates from 200 Mb/s to 2.5 Gb/s for distances up-to 65 cm. The presence of highly directional, linearly polarized, on-chip dipole antennas on the mm-wave radio along with the time division multiplexing (TDM) circuitry allows multiple wireless links to be created simultaneously with minimal inter-channel interference. This leads to a highly scalable solution for wireless MRI.

Index Terms

Close range; dipole antenna; horn antenna; imaging; impulse radio; IR-UWB; low power; mm-wave; MRI; OOK; optical transceiver; 60 GHz; wireless MRI

I. Introduction

Traditionally, MRI has always relied on a wired connection between the receiver coil array and the external processing circuitry to generate accurate images. To attain high image

quality, the number of receiver coil elements is increasing and separate receiver coil arrays are used for different parts of the body, resulting in increased cabling complexity. Today, 32 channels are common, and dedicated arrays exist for head, cardiac or abdominal imaging at most sites. The trend is toward even higher channel counts of 64 or more as these aid in parallel acceleration and simultaneous multi-slice spatial encoding [1], [2]. However, baluns and radio frequency (RF) traps are required for each channel and cables must be routed to minimize coil interactions. This leads to increased cost for operation and maintenance. Moreover, these receiver coil arrays are heavy and cumbersome as illustrated in Fig. 1(a), and can be intimidating and ill-fitting for children. The coil setup time can occupy a significant fraction of the total exam time. Consequently, removing these cables from the receiver coils could lead to a more cost effective and time efficient system, and ultimately enable light-weight, wearable coil arrays.

In the past, a number of architectures have been proposed to enable wireless MRI [3]–[8] for minimizing or removing the cables. All of these efforts used microwave frequencies up to 3 GHz, and protocols such as 802.11b or MIMO that are intended for long-range communication over distances of 10 m to 100 m. This results in a sub-optimal solution for wireless MRI in terms of power consumption and size. Typical MRI bore diameters vary from 60 cm to 70 cm. Depending on a patient's physical attributes and the part of the body to be imaged, the distance between the coil array and the magnet bore/edge can vary from 10 cm to 50 cm.

Here, we propose a custom millimeter (mm) wave transceiver architecture that meets the requirements for wireless MRI data rates at minimum power consumption and size. A block diagram is shown in Fig. II(b) in which the mm wave radio provides a short-range (10–50 cm) link within the MRI bore, and a fiber optic link transports data beyond the magnet to the console for image reconstruction. For a wireless array, the transmit logic state must also be broadcast (or RF power detected) to trigger on coil biasing of Q spoil switches [9] employing PIN diodes or even GaN FETs for negligible current bias [10]. The mm-wave data transmitter (TX) could be located on the MRI receiver coil assembly and the mm-wave data receiver (RX) embedded inside the MRI system bore. With the on-chip dipole antennas, the designed 60 GHz radio achieves a raw bit error rate (BER) of 10^{-6} for a distance of 10 cm, well in excess of the raw BER specification of 10^{-2} for a typical Wi-Fi, 802.11n system [11], [12] or 10^{-3} for a Bluetooth system [13]. For a TX-RX separation of 50 cm, the receiver is coupled with an external horn antenna and an LNA to compensate for higher signal loss at a longer transmission distance. We will describe the system design in Section II and experimental results in Section III, and discuss the findings in Section IV.

II. System Design

A. Design Overview

The wireless MRI data link consists of two main parts: a 60 GHz radio, and a fiber optic link. The radio transceiver operates in mm-wave frequencies with an RF carrier at 60 GHz using on-off key (OOK) modulation. The use of non-coherent modulation like OOK simplifies the system architecture as the TX and RX are not required to be phase synchronized. As the absolute phase of the system is not a concern, it relaxes the linearity

constraints for the power amplifier (PA) design, thus allowing the use of a more efficient non-linear PA. This reduces system power consumption allowing operation with small non-magnetic batteries. An earlier version of this transceiver was used for a short range, high data-rate, near field communication (NFC) system [14]. The transmitter consumed a best in class 5 pJ/bit over 10 cm due the OOK modulation and simplicity of architecture. The TX power of the new design scales from 1.3 mW to 14.0 mW as the data rate is varied from 200 Mb/s to 2500 Mb/s, while the RX consumes a fixed DC power of 76 mW and works up to 2500 Mb/s. The 60 GHz radio occupies a die area of 0.9×1.8 mm^2 (1.62 mm^2) and was designed and fabricated using a TSMC 40-nm 9-metal CMOS GP process.

B. 60 GHz Radio

The 60 GHz radio IC is comprised of a TX and an RX block. An on-chip dipole antenna is shared between the TX and RX blocks via a transmit-receive (TR) switch. The radio architecture along with signal waveforms at different points inside the TX and RX blocks is shown in Fig. 2. Significant changes were made from the prior design [14] to target MRI systems. As most of the commercially available analog to digital convertors (ADCs) for MRI provide a low voltage differential signaling (LVDS) output, an LVDS receiver was added to the radio baseband. Further, the baseband was modified to provide support for both return-to-zero (RZ) and non-return-to-zero (NRZ) signaling protocols. The previous version only supported RZ. This was done as the ADCs output is normally in NRZ format. Additional circuitry was added to enable clock and data synchronization between multiple transmitters. This allows multiple transmitters to be operated at the same time without interference, using built-in time division multiplexing (TDM) logic. Changes were also made to the power management circuit to minimize the leakage power. On the RF side, a dedicated TX was designed without the TR switch thus leading to higher drain efficiency for the PA. We only provide a brief overview of different circuit blocks here, as a detailed circuit analysis of different blocks would be beyond the scope of this paper.

1) Transmitter Block—The transmitter consists of a digital baseband followed by an RF front end. The digital data is fed to the transmitter baseband circuitry which supports both NRZ and RZ signaling protocols. The width of the RZ pulse can be programmed to assume any value from 250 ps to 1200 ps using a 6-bit pulse width controller (PWC). This RZ pulse is then fed to the transmitter radio RF front-end. The RF front-end consists of two identical TX elements each consisting of a voltage controlled oscillator (VCO), a power amplifier (PA), and an on-chip dipole antenna. To improve the on-chip antenna gain, the fabricated die was thinned down to 100 μm to minimize substrate losses and surface waves. The thinned die is mounted on a 600 μm thick FR4 printed circuit board (PCB) for measurements.

The VCO is a cross-coupled NMOS LC-oscillator and drives a class $E/F_{2,\ odd}$ PA with a simulated drain efficiency of 29%. The two VCOs and PAs are switched on and off, simultaneously, by the PWC modified RZ bit stream to generate impulse radio ultra-wide-band (IR-UWB) waveforms at the two dipole antennas.

2) Receiver Block—The receiver consists of an RF front end followed by a digital baseband. The RF front end consists of an on-chip dipole antenna followed by a 3-stage

transformer-coupled low noise amplifier (LNA). The LNA is an NMOS common source amplifier. The third stage of the LNA sums the received signals from the two dipole antennas, resulting in an improved signal sensitivity (point E). A passive AC-coupled self-mixer is used to extract the OOK modulation envelope (point F) which is then fed to the RX baseband. The RX baseband is a 3-stage DC-coupled inverter chain followed by a common-source amplifier with programmable resistive load. The last stage of the baseband is designed to drive an external 50 Ω load.

C. The Fiber Optic Link

The baseband data from the 60 GHz receiver in the MRI bore is transmitted over a fiber optic link to the MRI console room. This removes any possible RF coupling to the signal and also eliminates the need of RF traps on the signal path. The CMOS level, single-ended baseband data from the 60 GHz RX is converted to LVDS using a CMOS to LVDS translator (ON Semiconductor NB4N527). The LVDS data is then fed to an optical transmitter (Firecomms 1 Gbps LC transmitter). A plastic optical fiber (POF) carries the optical signal to the MRI console room. An optical receiver (Firecomms 1 Gbps LC receiver) recovers the electrical signal which is captured using a high speed sampling scope (Keysight Infiniium DSA91304A). This data is processed in MATLAB to recover the final test data. Though the Firecomms system is designed to support data rates up-to 1 Gb/s, initial testing revealed that there was considerable inter-symbol interference for data rates beyond 500 Mb/s. Thus testing inside the magnet was limited to 500 Mb/s data rates.

III. Evaluation

A. System Measurements inside the MRI Room

The MRI experiments were carried out on a GE 1.5 T Signa scanner. The aim of these experiments was to validate that a high data rate, mm-wave link can be established reliably inside the MRI magnetic bore in the presence of strong static magnetic field. Gradient coils and RF pulses were not enabled during these tests. Initial link tests employed an on-chip 7-bit pseudo random bit sequence (PRBS) generator to generate sufficient bit error statistics. Later tests demonstrated image transfer with specialized hardware.

1) Short Range Link Verification for 10 cm—Short link experiments tested for data integrity using only the on-chip dipole antennas. The short link setup and relative positioning of the TX and RX are shown in Fig. 3 and Fig 4(a), (b) respectively. A clock for the baseband PRBS generation in the 60 GHz transmitter was provided over plastic optical fiber by an RF signal generator (Keysight N9310A) located in the console suite. For the proof of concept experiment, the 60 GHz transmitter and receiver were placed coaxially with the magnet as shown in Fig. 4(c) or orthogonally (Fig. 4(d)). These orientations tested for Hall Effect [15] performance degradation relative to the static field. The data from the receiver was then transmitted over the fiber optic link to the scanner console room for further processing and BER calculations. Both orientations achieved BER $< 0.6 \times 10^{-6}$ thus demonstrating that the system performance is independent of its orientation inside the magnet. Fig. 5 shows the screen image of the 7-bit PRBS sequence as captured on the

sampling scope. The measured raw BER for different data rates and orientations at 10 cm is included in Table I.

2) Link Verification at 25 cm, 50 cm and 65 cm—For link distances greater than 10 cm, additional gain elements were added to the receiver chain as discussed in the Appendix I. A horn antenna placed before the 60 GHz radio receiver, coupled via a rectangular waveguide (WR-15), resulted in a link distance of 25 cm. The TX-RX distance was further increased to 50 cm and then to 65 cm by adding an external LNA to the horn antenna output using a 60 GHz coaxial cable as shown in Fig. 6. The LNA couples to the on-chip receiver antenna via a rectangular waveguide (WR-15). The TX, RX and Horn-LNA assembly were mounted on a custom designed slider made of MRI safe materials (Fig. 7). The slider allowed a variable distance between the TX and RX without disturbing the system component alignment.

Only axial orientations were tested given space restrictions, and the lack of detectable Hall effects in the prior experiments. The measured BER for different date rates and link distance is summarized in Table I. The sampling scope used for capturing the BER had a limited memory depth resulting in one million data points. Even after multiple data captures, no error was observed for any chunk of one million points resulting in a BER $< 1.0 \times 10^{-6}$.

The horn antenna used in the measurements at 25 cm and above has a 3 dB beamwidth of 24 degrees. Hence, even if the transmitter is not aligned with the receiver horn antenna, the system still meets the BER requirements up to a lateral distance of 5 cm. Beyond that, the BER starts degrading and goes below 1.0×10^{-3} for a lateral separation of 7.5 cm between the TX and RX axis of symmetry. This is important for an MRI system because a perfect alignment between the transmitter on a patient's body and the receiver embedded inside the MRI bore may not always be possible.

3) Image Transfer over 50 cm—Having established link reliability, a synthesized MRI image transmission was attempted over a link distance of 50 cm. The PRBS function was replaced by a base-band processing unit implemented in a FPGA board (Xilinx Kintex-7 FPGA KC705), and the data recovery processing was implemented in MATLAB. The baseband architectural details are highlighted in Fig. 8. An a-priori 256×256 MRI image was reformatted to 9 sub-blocks of fixed precision 16-bit real and imaginary pixels. The image blocks were serialized to a bit sequence, and converted to the RZ format. Lastly, run length limited (RLL) coding was applied. The latter operations prevent a DC offset build-up in the analog RF receiver circuitry which could corrupt the data.

The encoded bit streams were downloaded to the FPGA board memory. Upon external triggering, the binary data was transferred at 200MHz over POF to the mm-wave link inside the magnet, where it was envelope detected in the 60 GHz receiver at 50 cm separation, returned over a second POF link to the console room, and captured by a high speed sampling oscilloscope (Infiniium DSA91304A).

In MATLAB post-processing of the scope data, clock information was recovered from the oversampled digital samples, allowing correct bit alignment, and subsequent RLL decoding

of the bit stream and reformatting into image blocks. The segmented MRI image and the reconstructed image are shown in Fig. 9. The received image is an exact replica of the original image and no pixel errors were observed.

B. System Measurements outside the MRI Room

The 60 GHz radio can achieve much higher data rates, but was limited in-bore by the fiber optic channel limit of 500 Mb/s. To assess the true limits, the 60 GHz link was deployed outside the MRI, and the fiber optic cables were replaced by low loss SMA cables (Samtec RF316-01SP1-01SP1-0607) and high bandwidth baluns (ETS PI-102). Now, data rates to 2.5 Gb/s could be analyzed, and time domain multiplexing assessed.

1) Link Verification at 10 cm, 25 cm, 50 cm and 65 cm—BER tests were first repeated for 10–65 cm link distances using identical methods to those of section III-A.1 – III-A.2 with on-chip PBRS. The BER versus data rate for different distances is shown in Fig. 10. The measured BER is identical to that measured inside the MRI bore at the lower data rates. For all distances, BER increases as the data rate is increased. This is primarily due to finite receiver bandwidth and a higher inter-symbol interference as the data rate is increased.

2) Stress Test of the Link at 50 cm—Our BER statistical floor was limited to 10^{-6} by our instrumentation. As discussed in the Appendix I, the available link margin could possibly result in a much superior BER than the target value of 10^{-6}. Thus BER measurements were carried out using a bit error rate tester (Tektronix BERTScope Si 17500C, courtesy Marvell). The experiments were carried out using NRZ PRBS-7 at 2 Gb/s and 2.5 Gb/s. The real time eye diagram corresponding to a measured BER of 8.25×10^{-12} at 2 Gb/s for a distance of 50 cm is shown in Fig. 11. At 2.5 Gb/s, the BER dropped to 2.42×10^{-5}. The drastic degradation in BER after 2 Gb/s matches with the general waterfall curves for BER v/s energy per bit to noise spectral density E_b/N_0 [16]. The E_b/N_0 is related to SNR as

$$\frac{E_b}{N_o} = SNR \cdot \frac{B_w}{F_s}, \quad (1)$$

where F_s is the system data rate, and B_w is the channel bandwidth. As the system data rate goes up, E_b/N_0 falls, resulting in a higher BER. As data rates increase, the errors increases due to inter symbol interference, since more bits are packed closer and sent through the channel.

3) Time Domain Multiplexing (TDM)—As mentioned in Section II-B, the TX baseband supports TDM. Data from multiple transmitters can be received at a single RX without any interference. The test setup is shown in Fig. 12 where two TX units are placed with a lateral gap of 5 cm between them such that both are at a distance of 50 cm from the RX. Fig. 13(b) shows the screen shot of the initial received data for a data rate of 250 Mb/s. There is a significant overlap in the received data resulting in severe data corruption. Fig. 13(c) shows the same data after TDM is enabled in the TX baseband. There is no overlap between the data from different TX, thus the data from each TX can be reliably deciphered at the RX.

C. Power Consumption for Different Signaling Schemes

The 60 GHz radio supports multiple signaling schemes as mentioned in section II-B.1 Fig. 14 shows the TX power consumption for different modulation schemes as the data rate is varied from 200 Mb/s – 2500 Mb/s. The 60 GHz TX consumes DC power only while transmitting a data bit value of “1” because the TX is off while it is transmitting a data value of “0”. Thus, by using the PWC with RZ OOK, the power consumption of the TX scales with the data rate.

In addition to the data rate, the TX power consumption scales linearly with the pulse width. As shown in Fig. 2(c), the transmitter consumes power only during pulse width T when both the VCO and PA are turned on. It consumes only leakage power outside the pulse width T. The average DC power consumption of a single pulse is

$$P_{s_pulse}=\frac{T}{\tau}P_{pulse}=T\cdot data_{rate}\cdot P_{pulse}, \quad (2)$$

where P_{pulse} is the sum of both VCO and PA power consumptions and τ is the bit duration. A pulse width of 400 ps was used for measurements outside the MRI room resulting in a TX power consumption of 14 mW from a 1.1 V supply at 2500 Mb/s. This corresponds to an energy per bit of 5.6 pJ/bit for the TX. If the PWC is turned off, then the TX power consumption is almost constant for different data rates. The slight increase in power consumption with data rate is due to an increase in dynamic power consumption of the digital circuits.

As the receiver is always on, the power consumption is independent of the modulation type and the data rate. The RX consumes 76.8 mW of power from a 1.3 V supply.

IV. Discussion

The 60 GHz radio is just a first step towards the development of a wireless MRI system. Significant effort is needed for low power digitizing and decimation of the MRI coil data before transmission. A conventional MRI receiver chain of preamp, quad pipeline ADC and serializer (eg TI-TL5500, ADS5263, DS32EL0421) alone results in a DC power budget of 600 mW/element, and could easily reach 1W/channel once other control electronics are added. If a receive chain < 100 mW/channel were realizable by passive mixer down-conversion and SAR or continuous time sigma delta ADCs, one could envision a 32–128 channel wearable array supplied by non-magnetic battery or even wireless power delivery [17]. Present systems using 16 bit pipeline ADC sampling at 100 MS/s create raw data of 1.6 Gb/s for a single array element – a rate that would overwhelm Wi-Fi standards. By locally decimating to 500 KS/s (a high speed MRI case), 20 bit I/Q and 50% Rx duty cycle, a much more reasonable data rate of 10 Mb/s per element is achieved. Thus the required data throughput for a receiver array would vary from 320 Mb/s to 1280 Mb/s for 32 to 128 elements. These rates could rise even more as MRI transitions from 50 mT/m to newer 80 mT/m gradient systems.

The MRI bore is harsh electromagnetic environment and the channel behavior at 60 GHz, though expected, needed to be verified. Early research with 2.4 GHz devices using RSSI levels had shown significant multi-path in-bore because the wavelengths were of similar scale to body coil and shield separations and dimensions. The RF shield, in particular, prevents gradient eddy currents by being segmented with capacitive overlays to provide RF short circuits at 64/128 MHz, and presumably at GHz range. The Hall effect is known to influence preamplifier noise figure [18]-[20] and coil designers are careful to orient the preamp transistors to minimize this interaction [21] Lastly Sporrer et al. [22] discovered that gradient coil interactions significantly perturbed the frequency synthesis VCO of their in-bore receiver. This may be a concern for phase coherent modulation methods, if the QAM constellations are affected.

The very short range and specific timing needs of MRI seem well suited to low-complexity robust OOK modulation. Even so, the IEEE 802.11ac (5 GHz) and 802.11ad (60 GHz) standards must be considered. The 802.11ac standard actually has questionable scaling for MRI! We would consider single stream or at most 2 stream (dual antenna) per 802.11ac device as bore space and coil layout limit antenna deployment for MIMO. A Wi-Fi 80 MHz single stream channel using 256-QAM can support 433 Mbps (867 Mbps dual stream), but the actual throughput is at best about 67% or only 290 (580) Mbps. This barely suffices for small channel counts and cannot meet the maximum MRI channel counts and image bandwidths. The data throughput is contingent upon 256-QAM; if EM disturbances drop the link to even 64-QAM, data capacity is lost. The phase coherent modulations of 256-QAM orthogonal frequency division multiplexing (OFDM) in 802.11ac consume 1–2 watt at maximum rates [23], [24] versus 14 mW for 2.5 Gb/s OOK here. The nascent IEEE 802.11ad standard may in the long term be the most viable alternative for wireless MRI. With single carrier modulation, raw rates of 4.6 Gb/s are feasible in a 2.16 GHz wide channel with relatively low powers of 200–300 mW for 10 m range. Either standard would require embedded high level real-time operating system support to manage the protocols.

This work demonstrated that a high data rate, mm-wave link can be established reliably inside the MRI magnet bore in the presence of strong static magnetic fields. Gradients and RF pulses were not enabled since the added cabling needed for testing exposed the mm-wave radio to induced voltages that would not exist in its intended use. However, when a gradient echo (GRE) sequence was run with all cabling removed, the 60 GHz radio performance remained unaltered after later reconnection. We also expect that the OOK modulation, which does not require phase synchronous detection, will be more robust in the presence of gradient field perturbations, and optionally, data could be timed to transmit only in MRI RF-silent intervals if RF overload were an issue.

The minimum SNR is dictated by the required bit-error rate (BER). For non-coherent OOK, the receiver SNR must exceed 14 dB to get a raw BER < 10^{-6} [16] (before error correction or encoding). By comparison, the raw BER specification for 802.11n Wi-Fi and Bluetooth are 10^{-2} and 10^{-3} respectively [11]–[13]. From our link analysis (Appendix I), this was achieved with a 15dB link margin at 50 cm using the horn/LNA additions to the receiver. As per Eqn. 5, a 6 dB increase in receive antenna gain or decrease in receiver noise figure increases the link distance by a factor of 2. The target BER below 10^{-6} provides extra

robustness for frequency mismatch or antenna misalignment, flexibility in trading link margin for lower TX power, and simplified error correction coding.

The mm-wave radio offers significant flexibility in deployment. The design uses highly directional, linearly polarized, on-chip dipole antennas with 3 dB bandwidth of 50° [14]. Fig. 15 shows one concept in which one radio services a 4-coil module with quad ADCs and preamps. As a result, a 32-element coil could be formed using 8 of these modules. The dipoles can be placed orthogonally for nearest neighbor radios to significantly reduce cross talk. At 10 Mb/s for 500 kHz decimated MRI BW, each module would stream 40 Mb/s, but channel encoding and error correction will increase this rate further. For example, a ½convolution code would result in an effective data rate of 80 Mb/s. Second, the 60 GHz radio supports time division multiplexing (TDM) so multiple transmitters can be time interleaved to avoid data corruption in scenarios where the data from multiple transmitters is being collected at a single receiver. The radio also provides multiple options for clock and data synchronization between different transmitters. CMOS level clock signals can be physically routed to multiple transmitters and a 10-bit delay element in the baseband can be programmed to synchronize the data exiting different transmitters. This could be done as a onetime calibration for a particular set of transmitter receiver pairs. Finally, by connecting a loop antenna to the LVDS input port in the transmitter, a reference clock can be harvested by sending a pilot signal at any frequency, for example 2.4 GHz, inside the bore [14].

The proposed system should be easy to integrate in MRI systems. The small size transmitter with on-chip dipole antennas can be embedded inside the receiver coil array without influencing the MRI performance. When the radio chip is encapsulated in a dielectric assembly with a metal reflector as shown in Fig. 16, the radio antenna gain is simultaneously enhanced to 9.1 dBi [25] with a 3 dB bandwidth of 30°. On the receiver side, the horn-LNA-60 GHz radio assembly can be easily embedded inside the bore magnet, but similar gains and steerable sensitivity are ultimately best achieved by a beam steering 60 GHz receive array. Finally as the signal from the magnet to the console can be transferred over the fiber optic link, it will not couple and corrupt any existing RF signal in the magnet.

V. Conclusion

We have proposed a 60 GHz short-range radio system that offers a low power and scalable solution for wireless MRI digital links. As compared to analog transmission, digital transmission offers better noise immunity, stability and flexibility. The 60 GHz radio supports high data rates generated by commercially available ADCs designed to meet MRI dynamic range and SNR requirements. However, the 60 GHz radio is just a first step towards a complete wireless MRI system. Low power, high dynamic range ADCs tailored to MRI must still be developed but should be achievable with conventional technology. It has been over 2 decades since wireless MRI coils were first proposed. If these remaining subsystems can be realized, wearable wireless MRI receiver arrays could finally become reality.

Acknowledgments

The authors would like to thank TSMC University Shuttle Program for wafer fabrication and Firecomms for providing optical transceiver. Many thanks to Thomas Grafendorfer and Dr. Fraser Robb from GE Healthcare for

technical discussions. The authors are grateful to Lenin Patra and Vipul Chawla for their help in testing the system and the members of MRSRL for their support and understanding.

This work is supported by NIH grants R01EB008108, P01CA159992, R01EB019241 and GE Healthcare.

Appendix I

Link Budget Calculations

According to the Friis transmission equation [26], the received power P_r at distance R, for carrier wavelength λ, and transmitted power P_t is given by:

$$P_r = P_t G_t G_r \left(\frac{\lambda}{4\pi R}\right)^2, \quad (3)$$

where G_t and G_r are the transmit and receive antenna gains, respectively. The minimum received power required for a desired signal-to-noise ratio, SNR, is given by:

$$P_r = kT \cdot B \cdot F_r \cdot SNR, \quad (4)$$

where k, T, B and F_r are Boltzman constant, temperature in Kelvin, bandwidth of the receiver (bandwidth of the transmit pulse should be smaller than or equal to B), and the overall receiver noise factor, respectively. By substituting (3) into (4), the communication distance R becomes:

$$R = \sqrt{\frac{P_t \cdot G_t \cdot G_r}{kT \cdot B \cdot F_r \cdot SNR}} \left(\frac{\lambda}{4\pi}\right). \quad (5)$$

The choice of SNR is dictated by the required bit-error rate (BER). For non-coherent OOK modulation, the receiver SNR should be better than 14 dB to achieve a raw BER < 10^{-6} [16] (excludes error correction or encoding). In our implementation, the Tx/Rx antenna gains of the 2-dipole system are simulated to be 5.2 dB, hence by reciprocity $G_t = G_r = 3.31$ (5.2 dB). Since each PA radiates 4 mW, the total transmitted power through both PAs gives $P_t = 8$ mW. The receiver has noise factor $F_r = 1479$ (31.7 dB), and bandwidth B = 8 GHz. The TX bandwidth is programmable through the PWC with the maximum bandwidth at 8 GHz (corresponding to the narrowest pulse-width of 250 ps). Using $k = 1.38 \times 10^{-23}$ J/K, $T = 300$ K, $SNR = 25.1$ (14 dB), and $\lambda = 5$ mm, in (5) results in a link distance of $R = 10.6$ cm which barely meets the lower end of coil to magnet-bore distance requirement.

Even if the transmit antenna and power are maintained, link distance can still be increased by a higher gain RX antenna and preamplifier. A circular horn antenna (Ducommun ACH-14115-02) has 15 dB gain, 3 dB bandwidth of 10 GHz (58 GHz - 68 GHz) and 3 dB beam width of 24 degrees. By aligning the RX antenna with the horn waveguide, the link distance increases to R=33 cm, but is still short of our 50 cm goal. Next, consider adding a 60 GHz LNA (Spacek Labs SL6010). This LNA has a gain of $G_{LNA} = 31.6$ (15 dB), noise

factor, F_{LNA} = 3.98 (6 dB) and a 10 GHz (55 GHz -65 GHz) 3-dB bandwidth. With the external horn antenna and LNA, the receiver noise factor is now given by

$$F = F_{LNA} + \frac{F_r - 1}{G_{LNA} \cdot G_r}, \quad (6)$$

resulting in the effective receiver noise factor F=18.1 (12.6 dB), and yields a link distance of R=297 cm, well beyond the 50 cm goal. If we attempt to image the chest in a 60 cm bore diameter magnet, then the average distance between the patient's chest and the MRI bore is less than 10 cm. Thus 10 cm is sufficient if multiple mm-wave receivers are embedded in the bore. If the mm-wave receiver(s) are located near the bore edge (50 cm away), the longer range requires a higher gain antenna and LNA. The higher link distance results in additional power consumption by the external LNA and increases the area required to embed these components in MRI bore.

References

1. Zhang T, Grafendorfer T, Cheng JY, Ning P, Rainey B, Giancola M, Ortman S, Robb FJ, Calderon PD, Hargreaves BA, Lustig M, Scott GC, Pauly JM, Vasanawala SS. A Semiflexible 64-channel receive-only phased array for pediatric body MRI at 3T. Magnetic Resonance in Medicine. Sep; 2016 76(3):1015–1021. DOI: 10.1002/mrm.25999 [PubMed: 26418283]
2. Keil B, Wald LL. Massively Parallel MRI Detector Arrays. J Magn Reson. Apr.2013 29:75–89.
3. Murakami, Y., Tetsuhiko, T., Etsuji, Y. Nuclear magnetic resonanace inspection apparatus and its method. U.S Patent. 5,384,536. Jan 24. 1995
4. Boskamp, E., et al. Wireless RF Module for an MR imaging system. US Patent. 2003/020619A1. Nov. 2003
5. Scott, G., Yu, K. Wireless transponders for RF coils: systems issues. Proceedings of the 13th Annual Meeting of ISMRM; Miami, Florida, USA. 2005.
6. Riffe, MJ., et al. Using on-board microprocessors to control a wireless MR receiver array. Proceedings of the 17th Annual Meeting of ISMRM; Honolulu, Hawaii, USA. 2009.
7. Wei J, et al. A realization of digital wireless transmission for MRI signals based on 802.11 b. Journal of Magnetic Resonance. 2007; 186.2:358–363. [PubMed: 17433744]
8. Heid O, et al. CUTTING THE CORD-WIRELESS COILS FOR MRI. Proc Intl Soc Mag Reson Med. 2009; 17
9. Lu, J., Grafendorfer, T., Robb, F., Pauly, J., Scott, G. Proceedings of the 24th Annual Meeting of ISMRM. Singapore: May. 2016 Wireless Probe Detection for Auxiliary Control Syncing; p. 2180
10. Lu, JY., Aggarwal, K., Grafendorfer, T., Zhang, T., Robb, F., Pauly, J., Scott, G. High Powered GaN HEMT Devices for Low Powered Q-spoiling at 3T MRI. Proceedings of the 24th Annual Meeting of ISMRM; Singapore. May. 2016 p. 2175
11. Goldsmith, A. Wireless communications. Cambridge university press; 2005.
12. Peng F, Zhang J, Ryan WE. Adaptive Modulation and Coding for IEEE 802.11n. IEEE Wireless Communications and Networking Conference, 2007. Mar 11–15.2007 :656–661.
13. Gehrmann, C., Joakim, P., Smeets, B. Bluetooth Security. Colorado: Artech House Publishers; 2004. Artech House Computer Security Series
14. Taghivand M, Aggarwal K, Rajavi Y, Poon ASY. An Energy Harvesting 2 × 2 60 GHz Transceiver With Scalable Data Rate of 38– 2450 Mb/s for Near-Range Communication. IEEE Journal of Solid-State Circuits. Aug; 2015 50(8):1889–1902.
15. Hall E. On a New Action of the Magnet on Electric Currents. American Journal of Mathematics. 1879; 2(3):287–92.

16. Tang, Q., et al. IEEE International Conference on Communications. Vol. 4. IEEE; 2005. BER performance analysis of an on-off keying based minimum energy coding for energy constrained wireless sensor applications.
17. Byron, K., et al. RF Gated Wireless Power Transfer System. Proceedings of the 23rd Annual Meeting of ISMRM; Toronto, Ontario, Canada. 2015.
18. De Zanche, N., Roberts, B., Fallone, BG. Proceedings of the I8th Annual Meeting of ISMRM. Stockholm: 2010. Variation of Preamplifier Noise Figure with Bo Field Strength; p. 3916
19. Possanzini, C., Bouteljie, M. Proceedings of the 16th Annual Meeting of ISMRM. Toronto: 2008. Influence of magnetic field on preamplifiers using GaAs FET technology; p. 1123
20. Hoult, DI., Kolansky, G. Proceedings of the 18th Annual Meeting of ISMRM. Stockholm: 2010. A Magnetic-Field-Tolerant Low-Noise SiGe Pre-amplifier and T/R Switch; p. 649
21. Keil B, Blau JN, Biber S, Hoecht P, Setsompop V, Tountcheva K, Triantafyllou C, Wald LL. A 64-Channel 3T Array Coil for Accelerated Brain MRI. Magn Reson Med. 2013; 70(1):248–258. [PubMed: 22851312]
22. Sporrer B, Bettini L, Vogt C, Mehmann A, Reber J, Marjanovic J, Brunner DO, Burger T, Pruessmann KP, Trošter G, Huang Qi. Integrated CMOS Receiver for Wearable Coil Arrays in MRI Applications. Design Automation and Test Test in Europe Conference & Exhibition (DATE). 2015:1691–1694.
23. Saha SK, Deshpande P, Inamdar PP, Sheshadri RK, Koutsonikolas D. Power-throughput tradeoffs of 802.11n/ac in smartphones. IEEE INFOCOM. May.2015 :100–108.
24. Zeng Y, Pathak PH, Mohapatra P. A first look at 802.11ac in action: Energy Efficiency and interference characterization. IEEE IFIP Networking Conference. Jun.2014 :1–9.
25. Shafai, L. Encyclopedia of RF and Microwave Engineering. John Wiley & Sons, Inc.; Apr. 2005 Dielectric Loaded Antennas.
26. Friis HT. A note on a simple transmission formula. Proc IRE. 1946; 34:254–256.

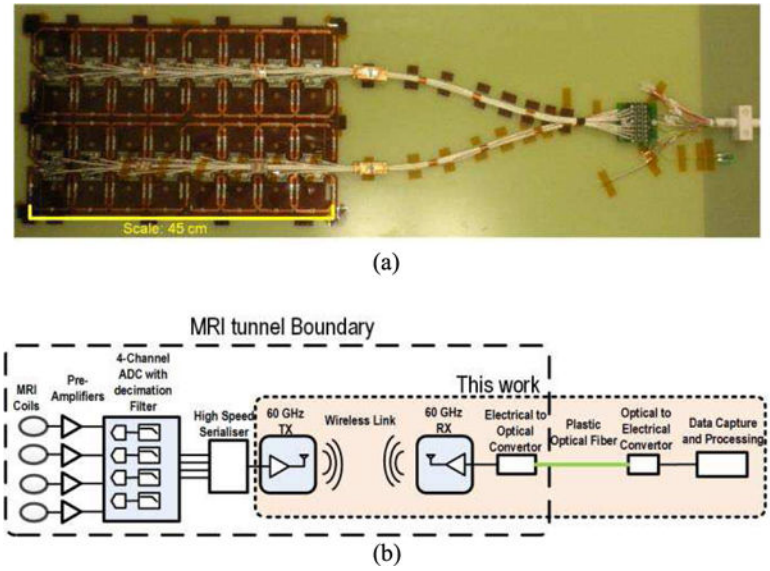

Fig. 1.

(a) A prototype 32-element receiver coil array with its associated cabling. (b) Proposed functional architecture for the mm-wave wireless MRI system along with the baseband required for digitization of MRI coil data.

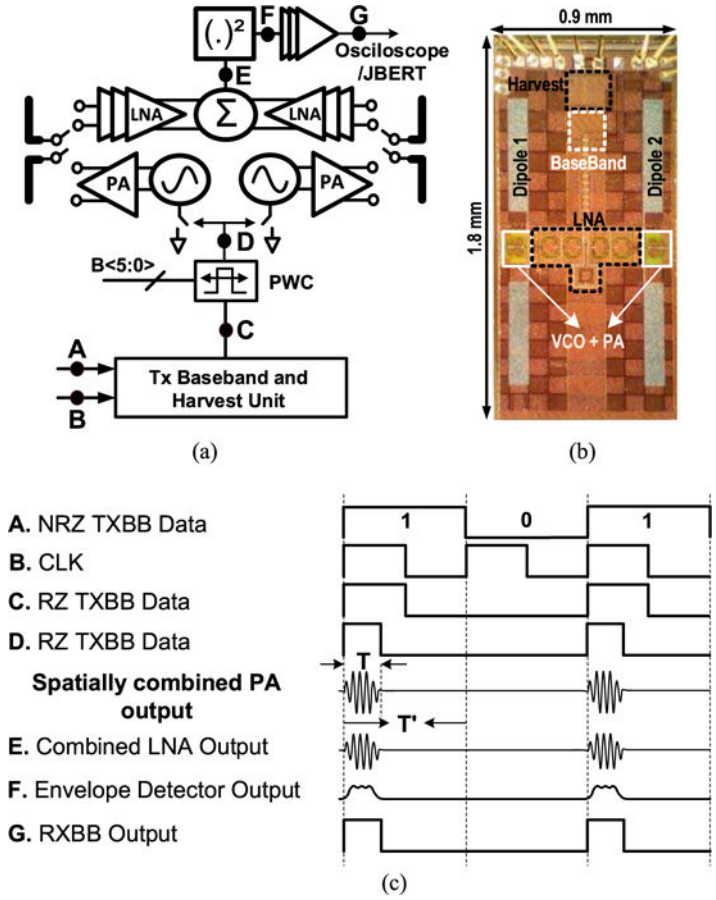

Fig. 2.

(a) mm-wave radio architecture, (b) the die photo of the manufactured 60 GHz radio, and (c) signal waveforms at different points inside the TX and RX.

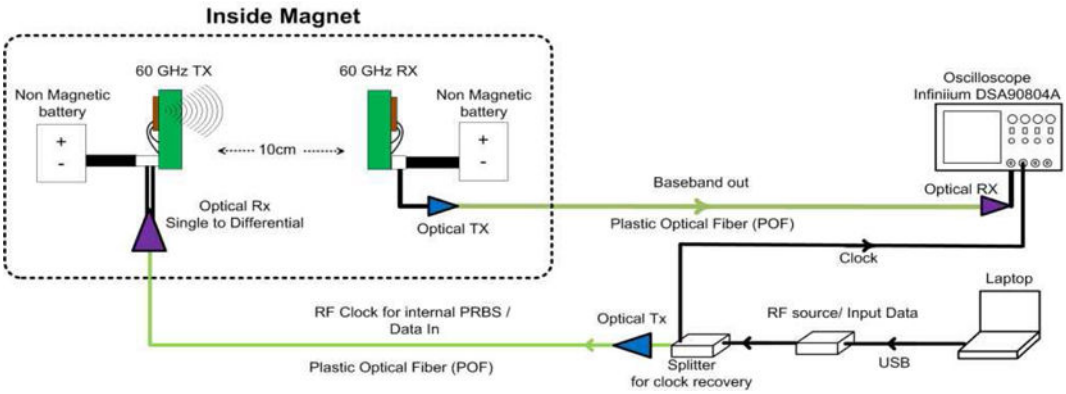

Fig. 3.

The block diagram showing the test setup for link verification inside the MRI room at a distance of 10 cm.

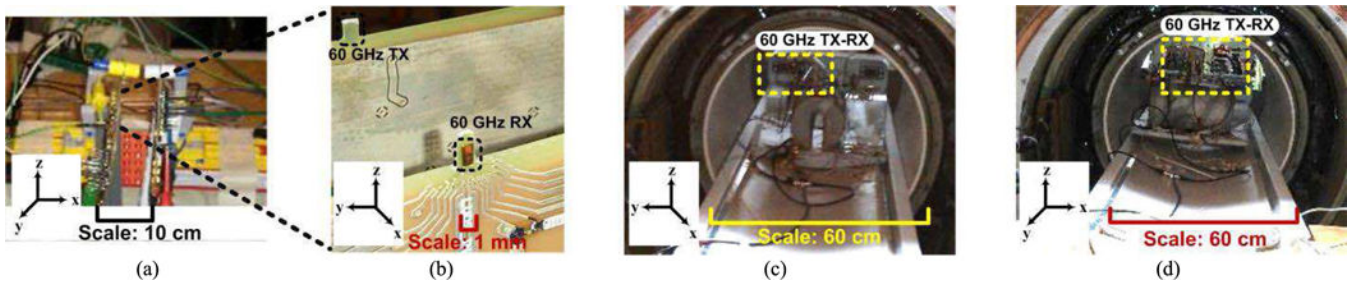

Fig. 4.

(a) The test setup showing the TX and RX alignment, and (b) a magnified view of PCB mounting the 60 GHz TX and the 60 GHz RX chip. The MRI test setup placed (c) in-line with the direction of the static magnetic field, and (d) perpendicular to the direction of the static magnetic field.

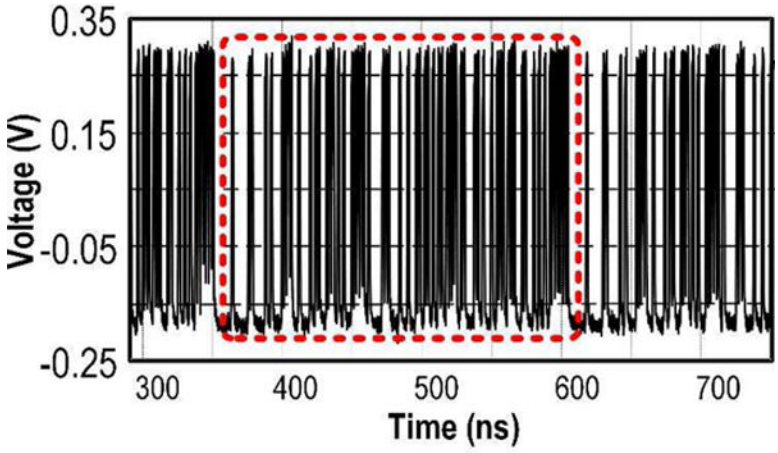

Fig. 5.

The 7-bit PRBS sequence as captured on the sampling scope at 500 Mb/s for a distance of 10 cm (voltage scale: 100 mv/div, time scale: 50ns/div). The repeated pattern is highlighted with dashed red box.

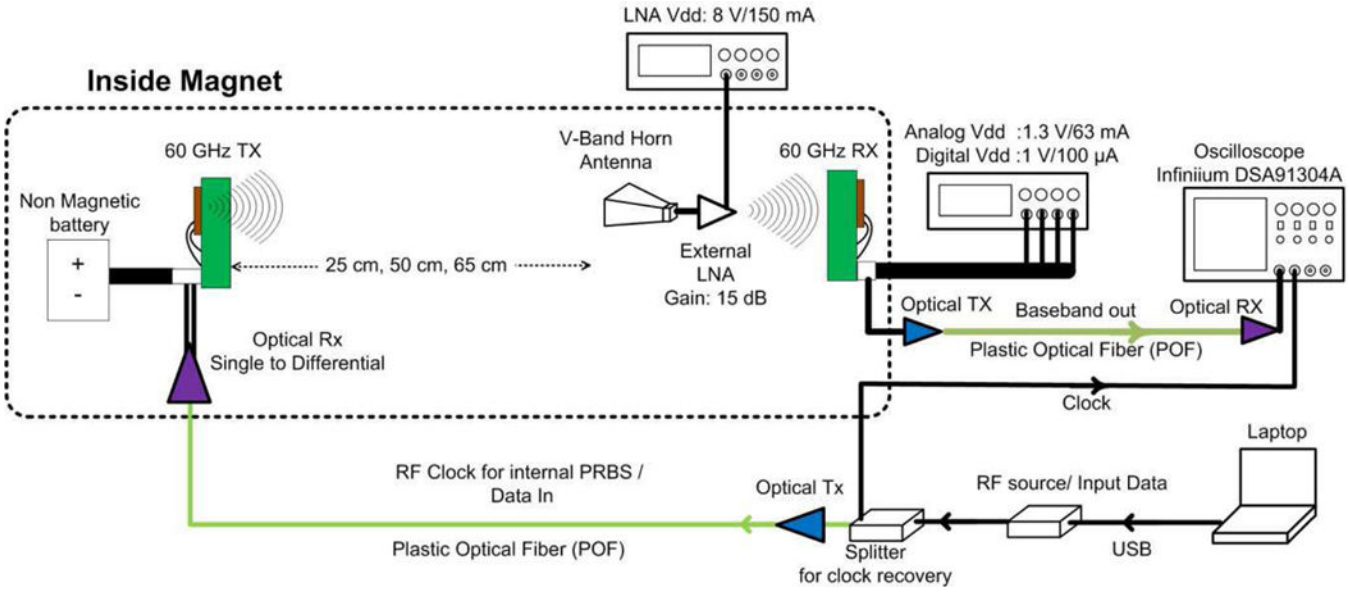

Fig. 6.

The block diagram showing the test setup for link verification inside the MRI room at a distance of 25 cm, 50 cm and 65 cm.

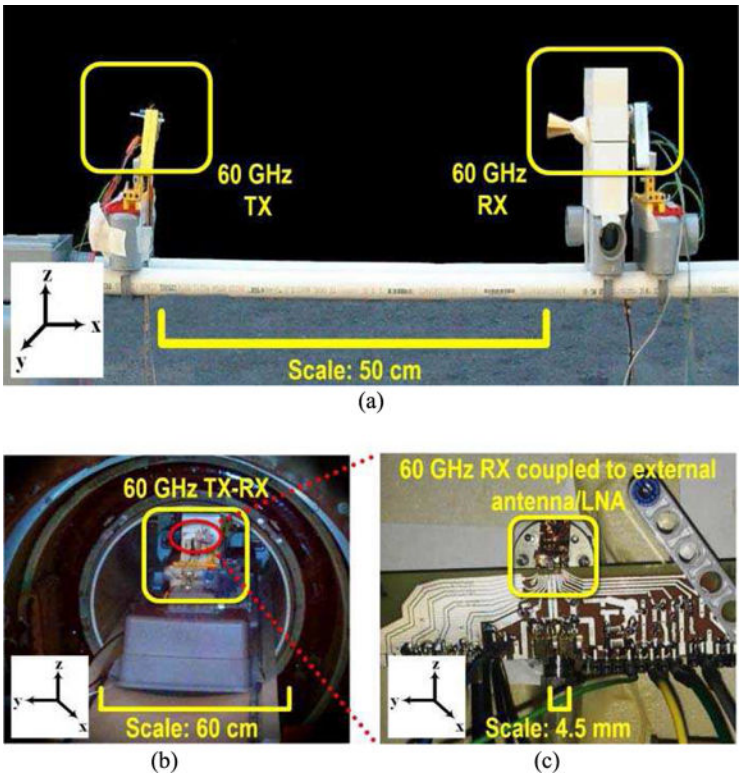

Fig. 7.

(a) The test setup showing the TX and RX alignment. (b) The test setup for 25 cm, 50 cm and 65 cm link placed inside the MRI bore. (c) 60 GHz Rx coupled to external antenna/LNA via waveguide output.

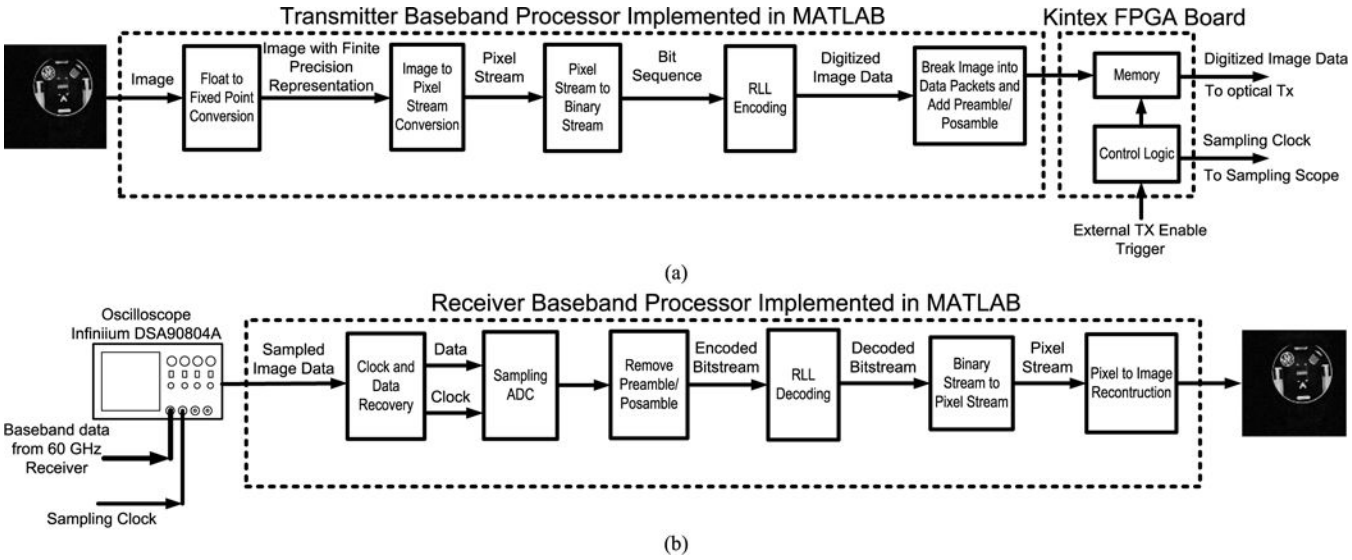

Fig. 8.

(a) The baseband processing unit implemented on the transmitter side, and (b) the baseband processing unit implemented on the receiver side for image processing.

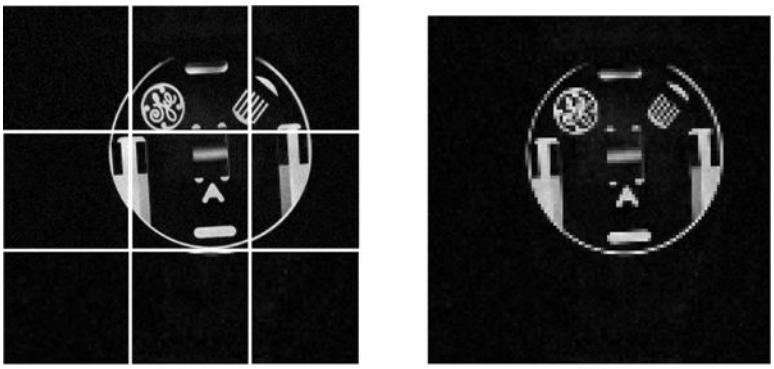

Fig. 9.

(a) The MRI image broken down into 9 pieces before transmitting through the system. (b) The received image after putting the pieces together.

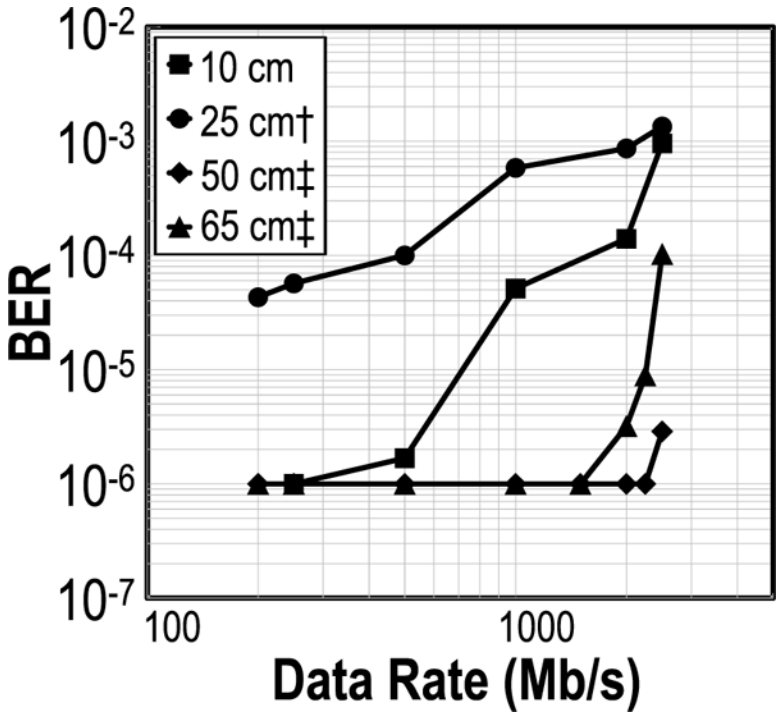

Fig. 10.

Bit-error rate versus data rate for 10 cm, 25 cm†, 50 cm‡and 65 cm‡. †An external horn antenna was placed in front of the receiver. ‡An external horn antenna followed by a LNA was placed in front of the receiver.

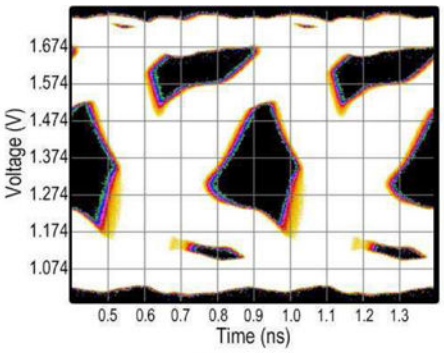

(a)

Results	
Total Bits	242,292,041,888
Total Bit Errors	2
Burst Related	0
Non-Burst Related	2
Total Bit Error Rate (BER)	**8.25e-12**
Burst Related	0.00E+00
Non-Burst Related	8.25e-12
Burst Events	0
Markers	0
Squelch Events	0
Pattern	PRBS-7
Settings	
Burst Minimum Length	32
Burst Error Free Threshold	32
Integration Period	1.00e+09 bits

(b)

Fig. 11.

(a) Real time eye diagram measured using the BERTScope at 2 Gb/s, and (b) the measured BER statistics at 2 Gb/s using PRBS-7.

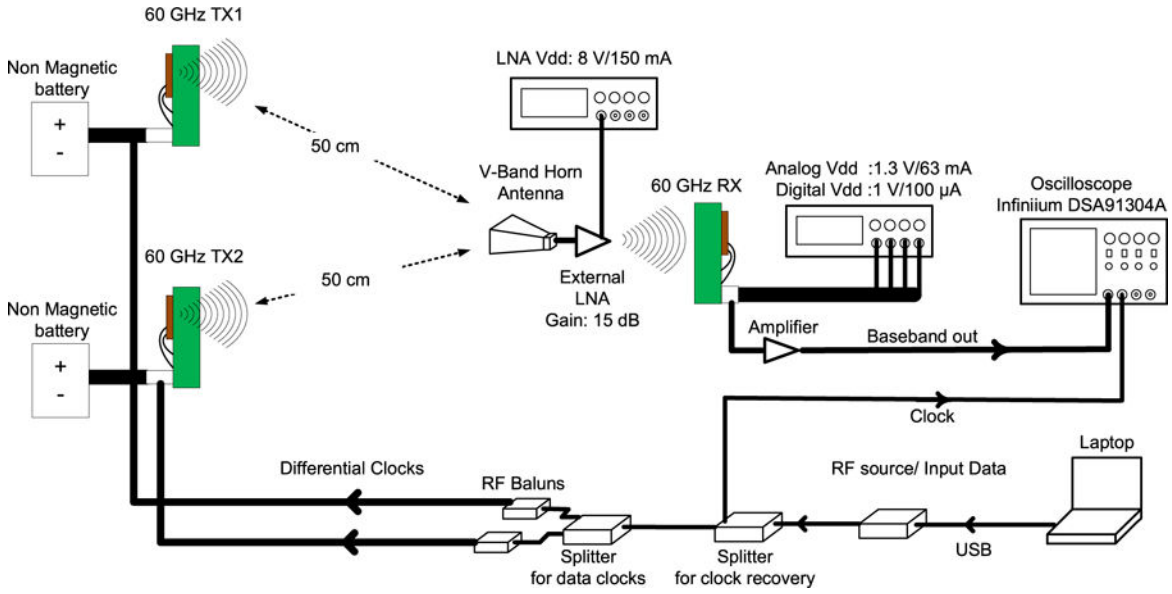

Fig. 12.

The block diagram showing the test setup for multiple transmitters at a distance of 50 cm from the receiver.

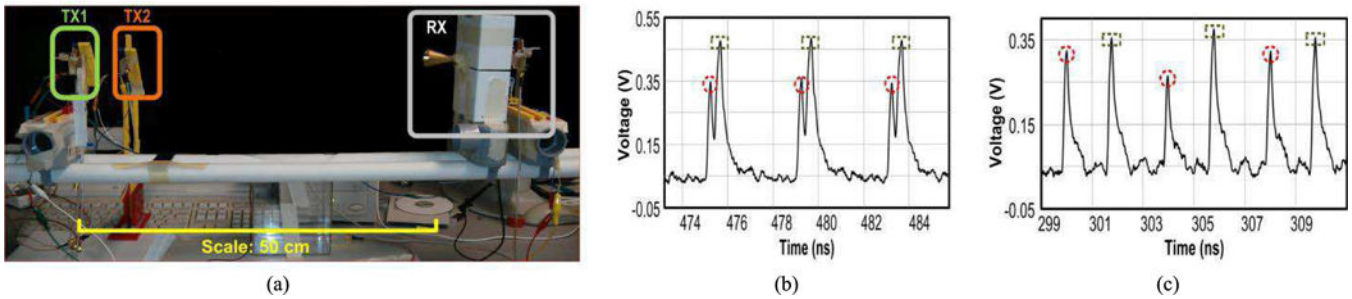

Fig. 13.

(a) The test setup for multiple TX to demonstrate time division multiplexing (TDM) at a data rate of 250 Mb/s and distance of 50 cm. Different shaped markers showing the received data corresponding to different transmitters when the (b) TDM block is turned OFF (voltage scale: 100 mV/div, time scale: 2 ns/div), and (c) when the TDM block is turned ON (voltage scale: 100 mV/div, time scale: 2 ns/div).

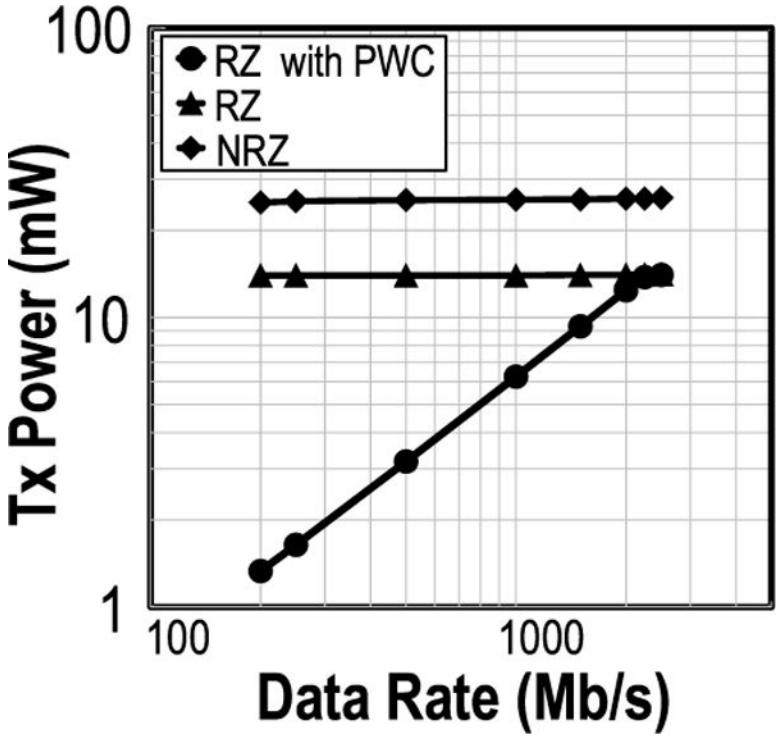

Fig. 14.
Transmitter dc power consumption versus data rate for different signaling schemes.

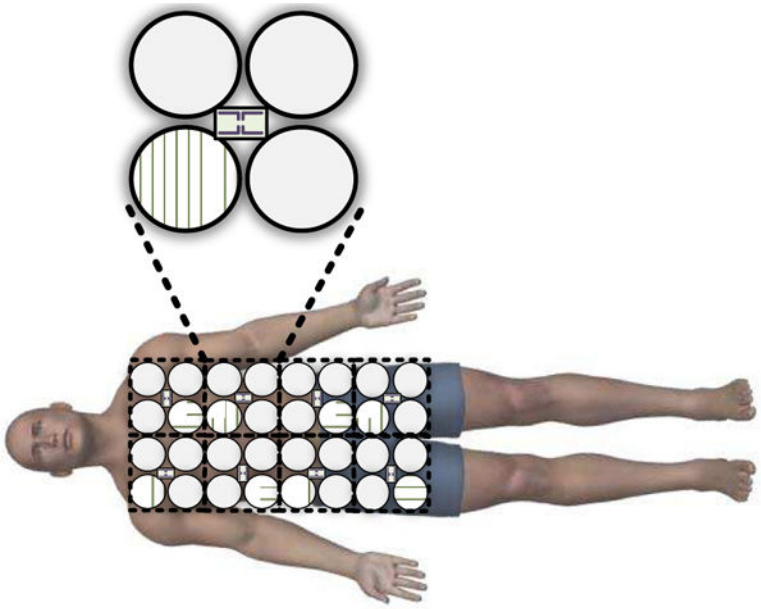

Fig. 15.

A 32-element receiver coil with 4-coil module sharing a single processing unit. Multiple 4 coil-modules are placed such that the RF transmitters in adjacent modules are orthogonal to each other, enabling multiple spatial streams.

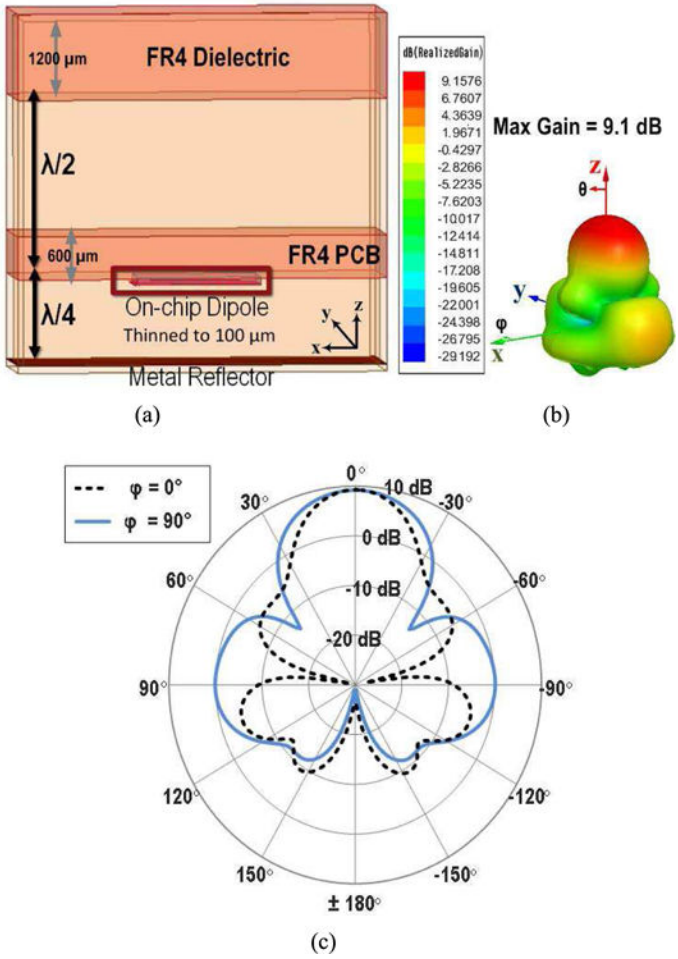

Fig. 16.

(a) 60 GHz radio with on-chip dipole placed inside an MRI safe package, (b) its HFSS simulated 3D radiation pattern with maximum gain of 9.1dBi, and (c) 2D radiation pattern for $\varphi = 0°$, and 90° as θ is swept from −180° to +180°. The metal acts as a reflector and enhances the gain of the dielectric-loaded antenna.

TABLE I

BER for different distance & data rates

TX-RX Distance	BER @200 Mb/s	BER @250 Mb/s	BER @ 500 Mb/s
10 cm	1×10^{-6}	1×10^{-6}	6.4×10^{-6}
10 cm*	1×10^{-6}	1×10^{-6}	4.8×10^{-6}
25 cm†	3.2×10^{-5}	3.9×10^{-5}	9.2×10^{-5}
50 cm‡	1×10^{-6}	1×10^{-6}	1×10^{-6}
65 cm‡	1×10^{-6}	1×10^{-6}	1×10^{-6}

*Setup was placed perpendicular to the external magnetic field as shown in Fig. 4 (d). All other measurements were taken by placing the setup inline to the external static magnetic field.

†An external horn antenna was placed in front of the receiver.

‡An external horn antenna followed by a LNA was placed in front of the receiver.